Noisy neuronal populations effectively encode sound localization in the dorsal inferior colliculus of awake mice.

Juan C. Boffi[1,3], Brice Bathellier[2], Hiroki Asari[3] & Robert Prevedel[1,3-6]

Affiliations

[1] Cell Biology and Biophysics Unit, European Molecular Biology Laboratory, Heidelberg, Germany.
[2] Institut Pasteur, Université Paris-Cité, INSERM, Institut de l'Audition, 63 rue de Charenton, F-75012 Paris, France.
[3] Epigenetics and Neurobiology Unit, European Molecular Biology Laboratory, Monterotondo, Italy.
[4] Developmental Biology Unit, European Molecular Biology Laboratory, Heidelberg, Germany.
[5] Molecular Medicine Partnership Unit, European Molecular Biology Laboratory, Heidelberg, Germany.
[6] Interdisciplinary Center for Neurosciences, Heidelberg University, Heidelberg, Germany.

Correspondence should be addressed to J.C.B. (juan.boffi@embl.de) and R.P. (prevedel@embl.de).

Abstract

The mammalian inferior colliculus (IC) is responsible for encoding sound location. However, the underlying neuronal population code at single-trial basis remains unclear due to the absence of large-scale simultaneous recordings. To address this knowledge gap, here we performed volumetric two-photon calcium imaging in awake mice and simultaneously recorded the activity of dorsal IC populations (~1,000 cells in size) in response to sounds delivered from 13 different frontal horizontal locations (azimuths). The recorded population responses revealed substantial trial-to-trial variability and noise correlations. Nevertheless, noise correlations helped decode stimulus azimuth effectively from these responses, reaching an accuracy matching that of the animal's discrimination ability. These findings demonstrate how correlated neuronal noise can improve the accuracy of a noisy population code, and support that single-trial population responses in the dorsal mammalian IC robustly encode sound location despite the inherent variation in responses from trial to trial.

Keywords

Volumetric calcium imaging, inferior colliculus, DCIC, sound location, population code, noise correlations.

Introduction

Locating a sound source facilitates essential behaviors such as foraging, mating and predator avoidance, thanks to the omni-directionality and long reach of the auditory system (*1*). In vertebrates, sound localization relies on both binaural cues such as interaural level and time differences (ILD, ITD) (*2*) and monaural cues including spectral notches (SN) (*3*). These sound localization cues are processed independently at brainstem nuclei in the ascending auditory pathway and integrated altogether for the first time at the inferior colliculus (IC) (*4*–*7*). This makes the IC a crucial early relay of the ascending auditory pathway to study how a primary neural representation of auditory space is formed (*4*, *5*).

Previous studies involving extracellular recordings from the mammalian IC revealed that average responses from IC neurons were tuned to multiple sound location cues, evidencing the integration of such cues at IC (*8*, *9*). However, the amount of sound location information carried by such individual neurons throughout the auditory pathway is limited and quite variable (*10*–*12*), suggesting that the sound location information is distributed into a population code for auditory space. Fundamental work by Day and Delgutte (2013) supports that sound location in the horizontal plane (azimuth) is represented at the mammalian IC by the activity patterns of populations of neurons that display average response tuning to azimuth, while ruling out other possibilities such as a topological code, an opposing two channel model or a population vector code (*13*, *14*). Nevertheless, this knowledge stems from prospective IC population activity patterns that were approximated by pooling non-simultaneous extracellular recordings and relied on extensive resampling of the pooled recordings to increase the number of “virtual” trials analyzed, under the assumption of independent firing between cells. Therefore, it remains an open question whether the actual activity patterns occurring in the IC of awake animals during single-trials can encode sound location given emerging properties such as correlated neuronal noise (*15*–*17*). Trial-to-trial response variability (neuronal noise) and neuronal noise-correlation can have a profound impact on the neural representations of sensory information, but this can only be determined through simultaneous large-scale recordings (*15*, *16*). Finally, traditional microelectrode recordings were mostly performed at a relatively deep anatomical subdivision of IC (central nucleus, CNIC), usually not targeting superficial regions (dorsal cortex, DCIC; external cortex, ECIC) (*8*, *12*, *18*–*20*). To overcome these limitations and explore the importance of trial-to-trial response variability, noise-correlation and dorsal IC populations on sound location coding, we performed large-volumetric Ca^{2+} imaging (*21*) and monitored DCIC population response patterns on the single-trial basis to interrogate the population code for sound location in passively listening awake mice.

Recent technical developments, including multichannel silicon probes (*22*) and fast volumetric Ca^{2+} imaging (*21*, *23*, *24*) enable routine simultaneous recordings from large numbers of neurons *in vivo*. Beyond their high throughput, volumetric methods are also a promising approach to precisely interrogate the topological distribution of neurons sensitive to sound azimuth, which has been reported to be random at CNIC (*18*), but is understudied at DCIC. In this work, we implemented scanned temporal focusing two-photon microscopy (sTeFo 2P) (*21*), an advanced volumetric Ca^{2+} imaging modality, to simultaneously record the activity of unprecedentedly large DCIC populations. Here we refer to DCIC as the dorsal IC region covering CNIC (*25*). Our approach produced direct evidence supporting that the response patterns from

mammalian DCIC populations effectively encode sound location on the single-trial basis in spite of their variability across trials. We also detected the occurrence of substantial noise-correlations which can contribute to the accuracy of this population code. Our findings point to a functional role of DCIC in sound location coding following a similar population coding mechanism to what has been proposed for CNIC (*18*). While CNIC is the main ascending relay carrying sound location information from brainstem auditory nuclei to the cortex through the auditory thalamus (*6*, *7*, *26*), DCIC is a higher order relay receiving profuse descending corticofugal inputs influencing auditory information processing including sound location (*27*–*30*). This knowledge sets forth exciting possibilities about the mechanisms by which cortico-collicular interactions affect relevant processes involving sound location information like leaning (*27*, *28*, *31*). More generally, these findings open new perspectives about the features of population responses that shape a sensory information representation on the single-trial regime, brought by cutting-edge recording modalities like sTeFo 2P that enable simultaneous high-throughput recordings.

Results

Simultaneous recordings of DCIC population activity:

In this work, we implemented sTeFo 2P for fast volumetric Ca^{2+} imaging, which enabled simultaneous sampling of the activity from unprecedentedly large DCIC populations. Moreover, TeFo based methods have been shown to be more resilient to highly scattering (optically opaque) tissues such as the IC (*32*). Adeno-associated viral vector (AAV) induced IC neurons expressing jRGECO1a (Fig. 1A) were imaged through a cranial window in awake head-fixed mice, passively listening to 500 ms-long broad-band noise stimuli (20-40 kHz white noise) delivered by a motorized speaker every 5 s located at one of 13 different frontal azimuth angles in a random order covering the frontal hemifield in 15º steps (Fig. 1B). We performed volumetric Ca^{2+} imaging (4 Hz volume rate) simultaneously sampling the activity of up to 2535 (643 ± 427, median ± median absolute deviation, n = 12 mice) regions-of-interest (ROIs) that had a shape and size consistent with an IC neuronal soma (12-30 µm diameter) (*33*), within a 470x470x500 µm volume from the right IC unilaterally, covering most of the dorso-ventral span of the anterior DCIC (Fig. 1A-C) and perhaps reaching the upper surface of CNIC below DCIC at more posterior locations (*34*). Since sTeFo 2P trades off spatial resolution for acquisition speed to produce volume rates compatible with the kinetics of Ca^{2+} sensors (voxel size: 3.7x3.7x15 µm) (*21*), we could not resolve fine spatial features of neurons such as dendrites or synaptic structures like spines in our images to unequivocally identify the segmented ROIs as individual neurons. For this reason, we refer to these ROIs as “Units”, in an analogous fashion to extracellular electrode recordings studies. To compensate for the relatively slow decay time of the Ca^{2+} indicator signal and non-linearities in the summation of Ca^{2+} events, we evaluated the spike probabilities associated to the neuronal Ca^{2+} signals (*35*) (Fig. 1D). The spike probability estimation does not involve predicting precise spike timings (*35*–*39*). Hence, we do not make any observation or interpretation in relation to the fine temporal structure of neuronal spiking. Instead, we treated the spike probabilities as a measure proportional to the spike count evaluated within the time interval set by our volumetric imaging rate (4 Hz). Taking into account that the main carrier of sound location information is IC neuron firing rate (*8*), we defined the evoked IC population responses as the mean spike probabilities of each imaged unit during the sound stimulation epoch (500 ms). In this way, we

systematically collected the simultaneous response patterns of IC populations to every azimuth trial. The IC populations simultaneously recorded from passively listening awake mice displayed spontaneous activity that was not time-locked to the stimulation (on-going activity) and sound-evoked response patterns that varied markedly across trials, as did the overall, average response of the complete imaged population (Fig. 1E).

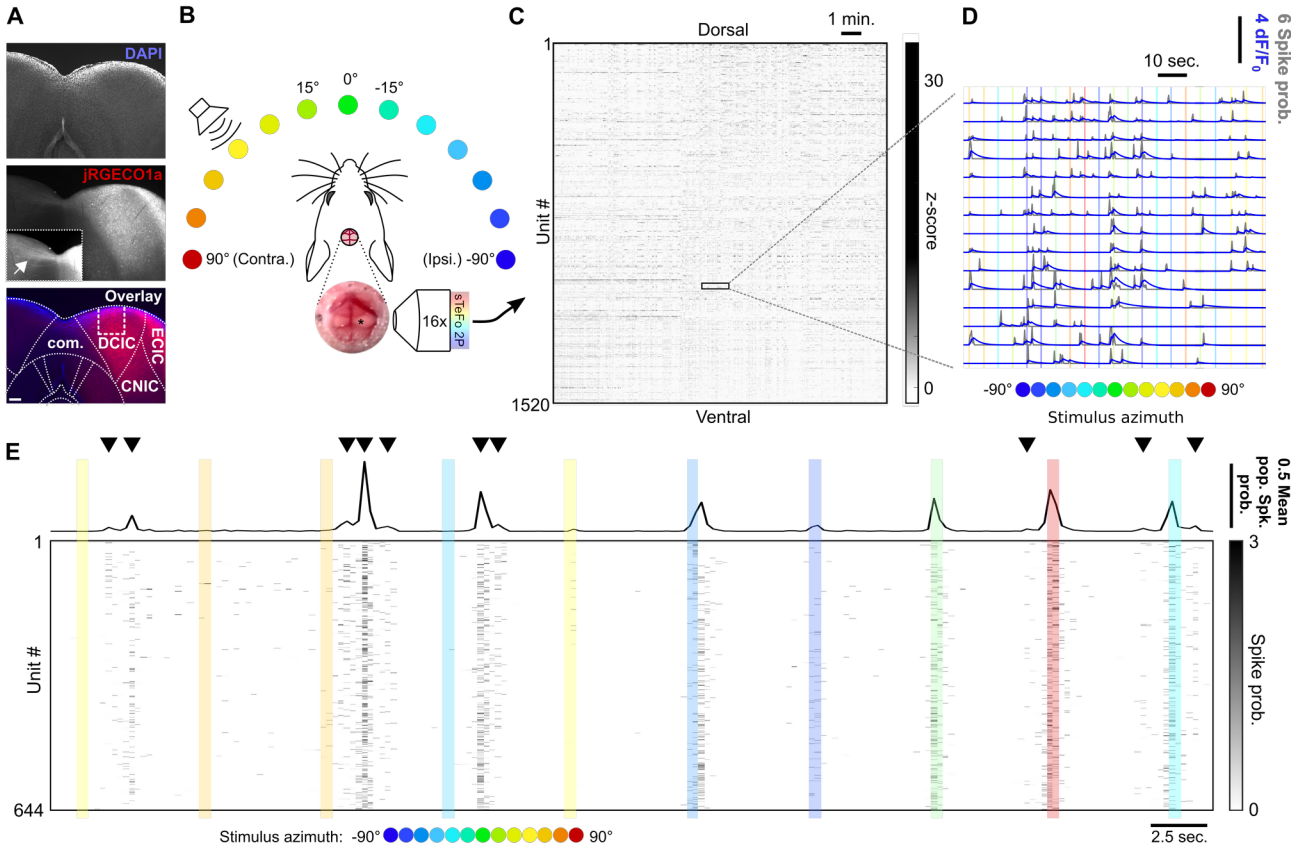

Figure 1: Simultaneous imaging of DCIC population responses to sound azimuth through sTeFo 2P. *In vivo* fast volumetric Ca^{2+} imaging of IC population activity. A) Representative histological section showing AAV induced jRGECO1a expression across IC. Middle panel inset: Contrast enhanced commissure region of the slice to visualize commissural projections from jRGECO1a expressing IC neurons. Bottom panel: Dotted lines delimit anatomical IC regions according to Paxinos et al. (2001); dashed lines delimit approximate area targeted for imaging. Scale bar: 200 µm. DCIC: dorsal cortex from inferior colliculus. CNIC: Central nucleus from inferior colliculus. ECIC: External cortex from inferior colliculus. Com.: Commissure from inferior colliculus. B) Schematic representation of the experimental design. Asterisk on the cranial window image marks AAV injection site. For reference, cranial window diameter is 4 mm. C) Neuropil-corrected and denoised jRGECO1a signals extracted from a representative full dataset. Extracted signals are arranged from dorsal (top) to ventral (bottom) ROI position across the IC volume imaged. D) Representative neuropil corrected and denoised jRGECO1a traces (blue) with their corresponding spike probability traces (gray) and stimulation epochs (color-coded based on stimulus azimuth angle according to (B)) super-imposed. E) Representative simultaneous recording of an IC population from an awake, passively listening mouse, displaying spontaneous, on-going activity (not synchronized to stimulation, arrowheads) and variable sound-evoked response patterns (during sound stimuli). Top trace is the population average response. Sound stimulation epochs are color-coded based on azimuth.

Decoding sound azimuth from single-trial DCIC population responses:

The observed trial-to-trial variability in our simultaneous, high-throughput Ca^{2+} imaging data raised the following question: To what extent do the single-trial responses of the DCIC units carry information about stimulus azimuth? To determine this, we first evaluated how accurately stimulus azimuth can be predicted from the complete single-trial DCIC population response patterns recorded in each imaging session (different mice), without taking resampling strategies or pooling recorded responses across animals or recording sessions as in the past studies (*18*, *40*). We performed cross-validated, multi-class classification of the single-trial population responses (decoding, Fig. 2A) using a naive Bayes classifier to evaluate the prediction errors as the absolute difference between the stimulus azimuth and the predicted azimuth (Fig. 2A). We visualized the cross-validated prediction error distribution in cumulative plots where the observed prediction errors were compared to the distribution of errors for random azimuth sampling (Fig. 2B). When decoding all simultaneously recorded units, the observed classifier output was not significantly better (shifted towards smaller prediction errors) than the chance level distribution (Fig. 2B). Given the high dimensionality of the dataset and the relatively low number of azimuth presentations collected, we reasoned that the classification failure could be due to overfitting rather than to a lack of azimuth information in the dataset. Thus, we tested if reducing the dimension of the dataset helps avoid overfitting. Specifically, we used the same decoder after dimensionality reduction through principal component analysis (PCA) with both PCA and classifier fit being cross-validated (Fig. 2C). We observed that decoding based on the first 20 to 40 principal components (PCs) produced absolute cross-validated single-trial prediction error distributions significantly better than the chance level distribution (Fig. 2 D, E); and that using larger numbers of PCs for model fitting and decoding decreased prediction accuracy (Fig. 2E). These results support that these DCIC responses indeed carry stimulus azimuth information which can be effectively decoded on a single-trial basis; and that the failure of decoding from the full population was merely due to overfitting.

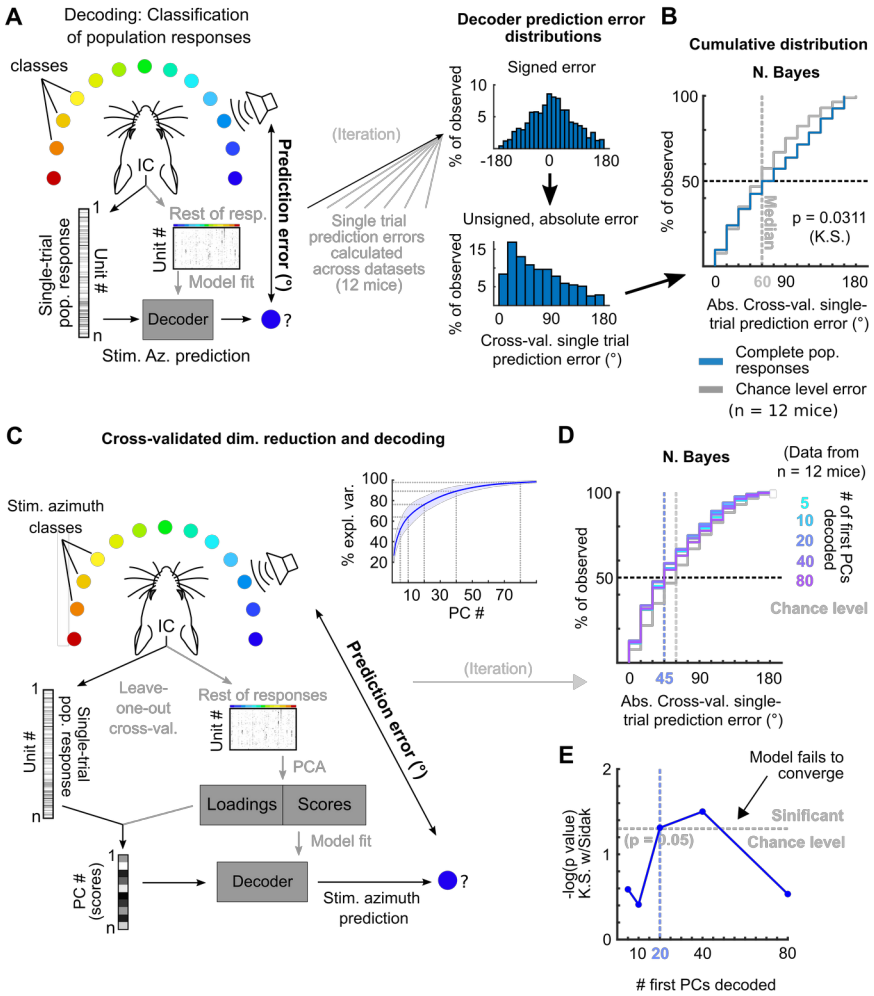

Figure 2: Decoding single-trial DCIC population responses to sound azimuth. A) Schematic representation of the decoding strategy using multi-class classification on the recorded simultaneous population responses. B) Cumulative distribution plots of the absolute cross-validated single-trial prediction errors obtained using naive Bayes classification (blue) and chance level distribution associated with our stimulation paradigm obtained by considering all possible prediction errors for the 13 azimuths tested (gray). K.S.: Kolmogorov-Smirnov test, n.s.: ($p > 0.05$). C) Schematic representation of the decoding strategy using the first PCs of the recorded population responses. Inset: % of explained variance obtained using PCA for dimensionality reduction on the complete population responses. Median (blue line) and median absolute deviation (shaded blue area) are plotted for (n = 12 mice/imaging sessions). D) Same as (B) but for decoding different numbers of first PCs from the recorded complete population responses. E) Significance of classification accuracy with respect to chance level for different numbers of first PCs, determined via Kolmogorov-Smirnov tests with Sidak correction for multiple comparisons. Arrowhead indicates model loss of performance associated with fitting more parameters for a larger feature space (# PCs) with the same dataset size (# trials collected).

Sound azimuth information is carried redundantly by specific DCIC units:

The decoded PCs consist of linear combinations of the responses from the units in the imaged DCIC population. Then the following questions arise: To what extent is the sound azimuth information distributed across the imaged DCIC populations? Is it fully distributed across most units or specific to some of them, such as azimuth tuned neurons?

To investigate the aforementioned questions, we next asked if any fraction of the recorded DCIC units carried more azimuth information in their responses than other neurons. First, we calculated the signal-to-noise ratio for the responses of each unit ("neuronal" S/N, nS/N), defined as the ratio between the mean

(signal) and the standard deviation (noise) of the responses to the unit's best azimuth. Imaged DCIC units generally showed a relatively low nS/N during sound stimulations (< 1, Fig. 3A). Nevertheless, this nS/N was significantly larger than the one registered in the absence of sound stimulation (on-going activity from the periods between sound stimuli, Fig. 1E, 3A), indicating that sound responses across the sampled units were often noisy. However, the broad distribution of nS/N also suggested that a sparse population of neurons responded more robustly. Next, we evaluated azimuth tuning to delimit subpopulations with higher azimuth selectivity. Using non-parametric one-way ANOVA (Kruskal-Wallis test), we identified the imaged units whose median responses changed significantly based on stimulus azimuth, which we defined as azimuth tuned units (Fig. 3B). The units with significant azimuth tuning represented only 8 ± 3% (median ± median absolute deviation, n = 12 mice) of the DCIC units simultaneously-imaged in one session (mouse; Fig. 3C). This is not significantly different from the false positive detection rate of our ANOVA tests ($\alpha = 0.05$, Fig. 3C). Given that a large number of trials showed no response at all in many units, it is possible that the large trial-to-trial variability in the imaged DCIC responses made it difficult to detect response specificity based on differences in median activity. We thus employed more sensitive χ^2 tests to determine the statistical dependence between the recorded DCIC responses and presented stimulus azimuth. We then ranked the units in our simultaneously imaged samples based on the p-value of the χ^2 tests (Fig. 3D) to delimit subsamples of DCIC units showing the strongest azimuth-dependent responses. The units with significant response dependency to stimulus azimuth ($p < 0.05$) represented 32 ± 6% (median ± median absolute deviation, n = 12 mice) of the units simultaneously-imaged in one session (mouse, Fig. 3E). Even the top ranked units typically did not respond in many trials; nevertheless, their evoked responses showed a tendency to be more selective towards contralateral or central stimulus azimuths (Fig. 3D, inset).

To test if the single-trial response patterns from simultaneously imaged units with top response dependency to stimulus azimuth carry enough information to generate better azimuth predictions than the ones observed with the complete samples (Fig. 2), we evaluated the prediction errors obtained by decoding them. In doing so, we cross-validated both unit ranking based on response dependency (feature selection) and decoder fit (Fig. 3F). From this point on, we will refer to groups of units showing maximum response dependency to stimulus azimuth as "top ranked units". To evaluate the minimum number of top ranked units necessary to generate stimulus azimuth predictions significantly better than the chance level, we decoded different sized subsamples of these units. We found that the single-trial response patterns of at least the 7 top ranked units produced stimulus azimuth prediction errors that were significantly smaller than chance level ($p = 6 \times 10^{-4}$, Kolmogorov-Smirnov with Sidak) using Bayes classification (naive approximation, for computation efficiency) (Fig 3G). Increasing the number of top ranked units decoded did not bring major improvements in decoder performance (plateau), up to a point where performance dropped, due to classifier overfitting caused by the relatively small number of collected trials per class (Fig 3G, bottom). If we consider the median of the prediction error distribution as an overall measure of decoding accuracy, the single-trial response patterns from subsamples of at least the 7 top ranked units produced median decoding errors that matched the reported azimuth discrimination ability of mice (Fig 3G, minimum audible angle = 31º) (*41*). Altogether, despite the trial-to-trial variability in the imaged IC activity, these results represent direct evidence supporting that the single-trial response patterns from subpopulations of mammalian DCIC units with maximum

response dependency to stimulus azimuth constitute a population code for sound location. These subpopulations are constituted by around 32% of the imaged DCIC populations, out of which a small number of them are sufficient for achieving the best decoder performance. Altogether, these results suggest that sound location information is distributed throughout many DCIC units in the imaged populations (top ranked units, ~32%) rather redundantly, as a small number of these units are sufficient to decode sound azimuth matching behavioral accuracy.

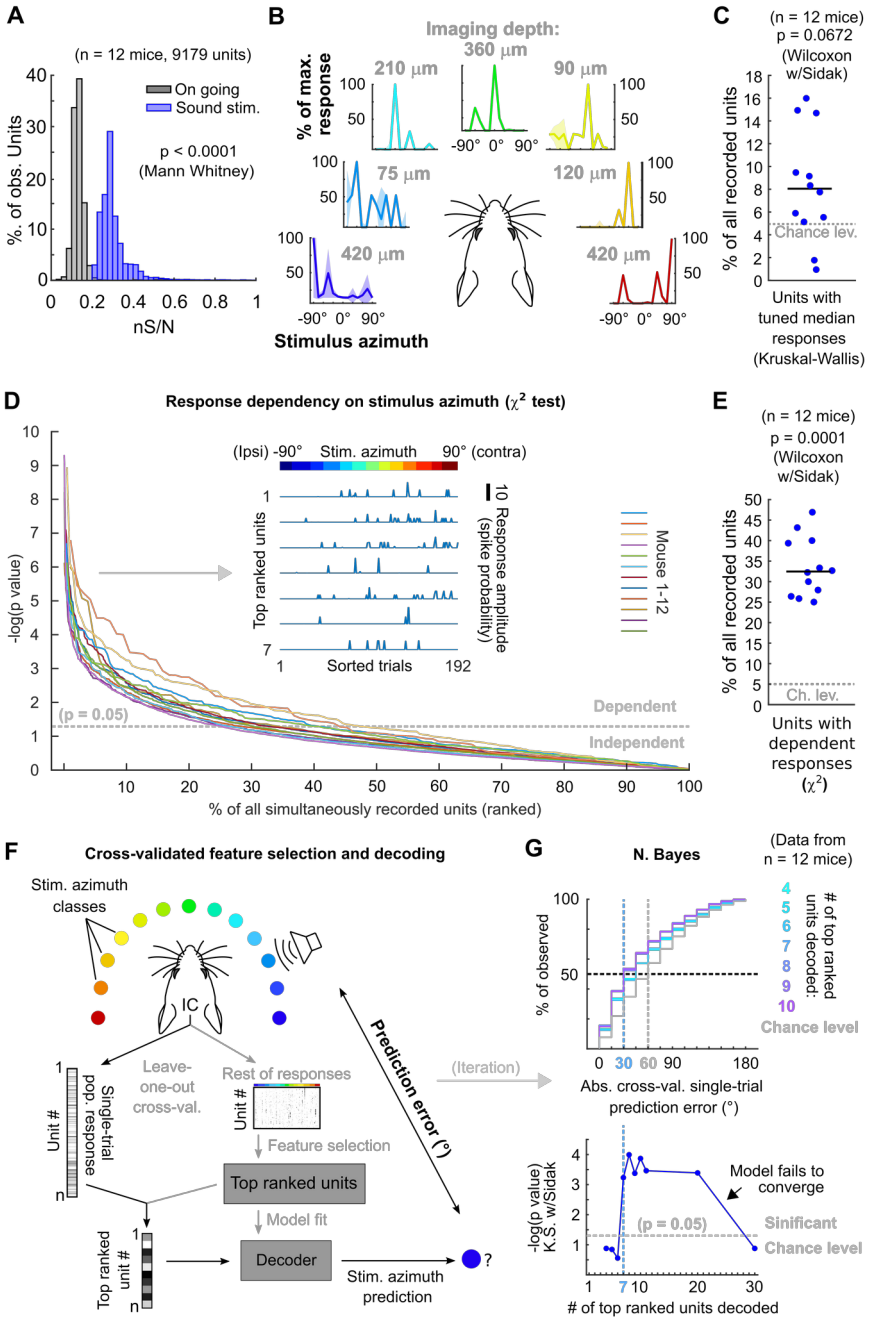

Figure 3: Sound azimuth information is carried by specific units from the imaged DCIC populations. A) Histogram of the nS/N ratios from the recorded units across mice during sound stimulation or during the inter trial periods without sound stimulation (on going). B) Representative stimulus azimuth tuning curves from units with significant median response tuning detected using non-parametric one way ANOVA (Kruskal-Wallis test). Median and absolute median deviation are plotted. The imaging depth from the corresponding units is displayed in gray. Azimuth selectivity is color-coded based on Fig. 1B. C) Percentage of the simultaneously recorded units across mice

that showed significant median response tuning, compared to false positive detection rate (α = 0.05, chance level). D) Response dependency to stimulus azimuth, determined via χ^2 tests (see methods), for simultaneously recorded units ranked in descending order of significance. Inset: Representative responses from the top ranked 7 units with significant response dependency to stimulus azimuth. Response amplitudes are displayed with a continuous trace for visualization purposes, the displayed response order was sorted as a function of stimulus azimuth and does not represent the experimental stimulus delivery order (random). E) Percentage of the simultaneously recorded units across mice that showed significant response dependency to stimulus azimuth, compared to false positive detection rate (α = 0.05, chance level). F) Schematic representation of the decoding strategy using the top ranked units from the recorded population responses. G) Top: Cumulative distribution plot of the absolute cross-validated single-trial prediction errors obtained with a Bayes classifier (N. Bayes, naive approximation for computation efficiency). The number of top ranked units considered for decoding their simultaneously recorded single-trial population response patterns is color coded from cyan (4 top ranked units) to purple (10 top ranked units) and the chance level distribution associated to our stimulation paradigm, obtained by considering all possible prediction errors for the 13 azimuths tested, is displayed in gray. Bottom: Significance of classification accuracy with respect to chance level for 4 to 30 decoded top ranked units, determined via Kolmogorov-Smirnov tests with Sidak correction for multiple comparisons. Arrowhead indicates model loss of performance associated with fitting more parameters for a larger feature space (# units) with the same dataset size (# trials collected).

Noise correlations contribute to the population code of sound azimuth at DCIC:

In our simultaneous recordings we observed the occurrence of time correlated peaks of activity across pairs of units (Fig. 4A). This observation points out to an important factor affecting population codes under large trial-to-trial response variation: neuronal noise correlation (*15*, *16*), which has been previously reported to occur at mammalian IC populations (*17*). Here, we interpreted neuronal noise as the variability of each unit's responses across trial repetitions for a certain stimulus azimuth. We evaluated the Kendall Tau as an unbiased, non-parametric pairwise correlation coefficient for the neuronal noise from all possible pairs of simultaneously recorded DCIC units across trial repetitions for each stimulus azimuth. Using cross-validated hierarchical clustering of the simultaneously imaged units based on noise correlation, we observed no clear groups (clusters, subpopulations) of highly noise correlated units across the trial repetitions from each stimulus azimuth (Fig. 4B). Nevertheless, the pairwise noise correlation coefficients observed across datasets (mice) showed a distribution that was significantly shifted towards positive values with respect to chance level, calculated from the same datasets subjected to randomization of each unit's responses across trial repetitions for each stimulus azimuth (Fig. 4B). Evaluating pairwise correlations in the on-going activity of the simultaneously imaged units, recorded during the inter-trial periods without sound stimulation, showed a similar outcome (Fig. 4B). This significant shift towards positive values suggests that noise correlations (during sound stimulation) and correlations in on-going activity (without sound stimulation) could be associated with or reflecting similar underlying processes. Finally, the same observations were met when focusing on the top ranked units (~32% from the complete DCIC populations imaged, Fig. 4C), pointing out that the observed noise correlations are indeed present in the DCIC subpopulations associated with the population code for sound azimuth.

The observed more frequently positive noise correlations could affect the representation of stimulus azimuth by population responses in different ways (Fig. 4D). To characterize this, we first qualitatively visualized how the noise correlations affected population response separability (Fig. 4D) using dimensionality reduction through linear discriminant analysis (LDA). This supervised method of dimensionality reduction allowed us to define dimensions along which the single-trial responses from the simultaneously imaged subpopulations of

top ranked units should segregate maximally across stimulus azimuth classes. We cross-validated the LDA following the same leave-one-out strategy as with the PCA (Fig. 2C), in which linear discriminant (LD) coefficients were determined for all except one trial response and the LD scores for this response were calculated with the fitted LD coefficients. The scatter from these responses in 2D LD space showed little to no segregation across the 13 different stimulus azimuths tested (Fig. 4E). This suggests that the representation of stimulus azimuth by these responses is complex and likely of higher dimensionality. In consequence we embedded the responses projected across 12 linear discriminant dimensions (for 13 azimuth classes) into a 2D manifold using the uniform manifold approximation and projection (UMAP) (*42*) (Fig. 4F). This revealed that the responses clustered and segregated from the rest for some azimuths, but overlapped to different extents for the other azimuths (Fig. 4F). We studied how these responses would segregate across azimuth classes in the absence of noise correlations by modeling decorrelated datasets through randomization of each unit's responses across trial repetitions for each stimulus azimuth (within-class randomization, Fig. 4G) in our simultaneously imaged datasets. The scatter from these modeled decorrelated responses qualitatively resembled the chance level scatter observed for datasets with scrambled responses (Fig. 4G, H).

To produce a more quantitative estimation of the influence of noise correlations on the population code of sound azimuth at DCIC, we compared the decoding accuracies obtained by classifying the single-trial response patterns from top ranked units in the modeled decorrelated datasets versus the acquired data (with noise correlations). Using the Bayes classifier (naive approximation, for computational efficiency), we observed that the modeled decorrelated datasets produced stimulus azimuth prediction errors that were not significantly different from chance level (Fig. 4I) and significantly larger than the ones observed with the recorded data (with noise correlations, $p < 0.0001$ Kolmogorov-Smirnov, w/Sidak). Altogether, these results suggest that the detected noise correlations in our imaging datasets help improve the accuracy of the IC population code for sound azimuth by affecting the separability of the single-trial response patterns of top ranked units across azimuth classes.

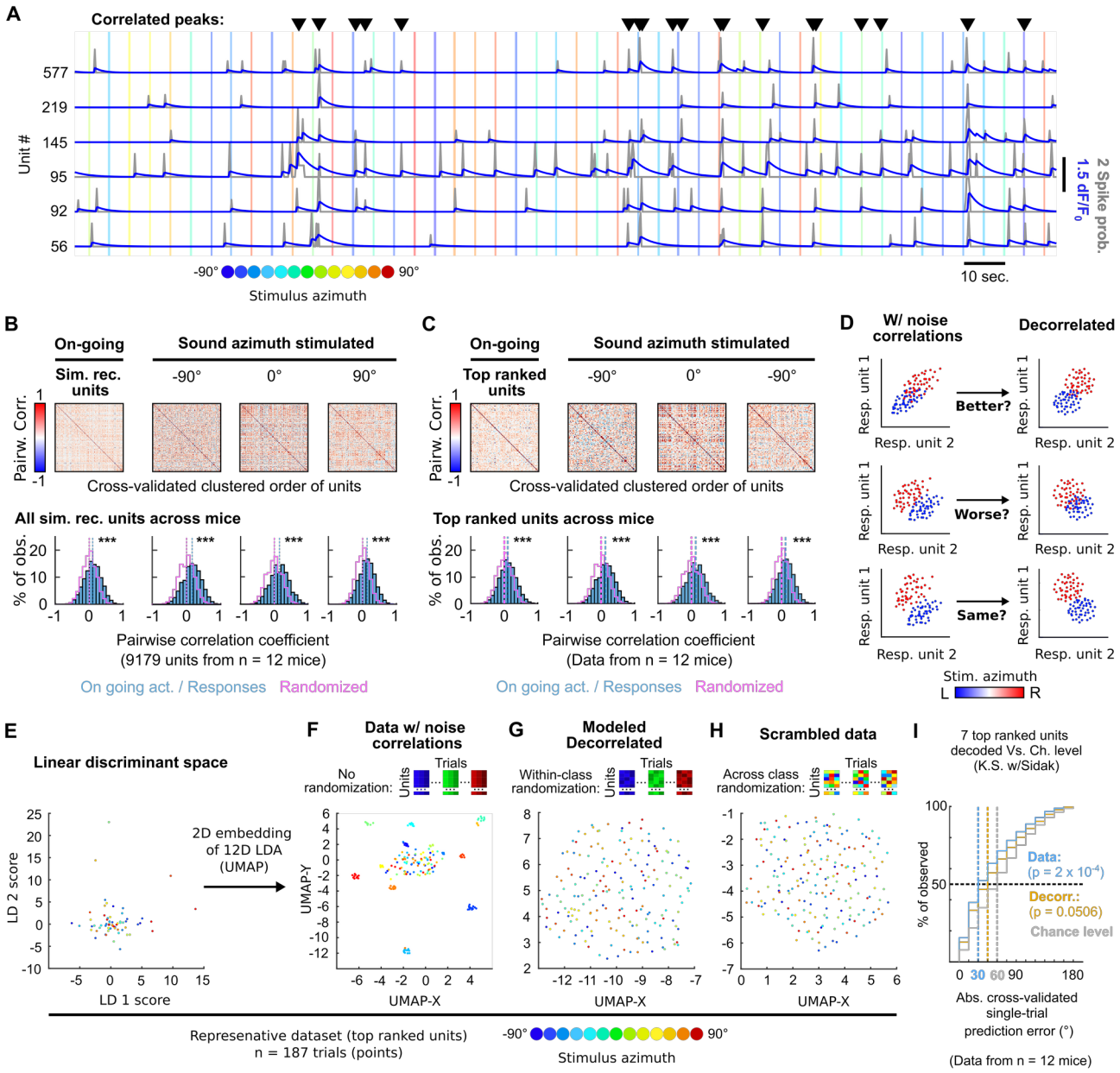

Figure 4: Noise correlations in DCIC population activity contribute to encode sound azimuth. A) Representative recordings from selected units displaying time correlated activity peaks. Arrowheads mark the timestamps of detected correlated peaks. B) Top: Representative correlation matrices of pairwise correlations detected in simultaneous recordings during inter trial periods (without sound stimuli, on-going) and during sound stimuli for representative azimuths. The simultaneously imaged units are sorted in the correlation matrices based on cross validated hierarchical clustering (see methods). Bottom: Distribution histograms for the pairwise correlation coefficients (Kendall tau) recorded from simultaneously recorded units across mice (blue) compared to the chance level distribution obtained through randomization of the temporal structure of each unit's activity to break correlations (purple). Vertical dashed lines show the medians of these distributions. C) Same as B but for the 30 top ranked units across datasets (mice).***: $p < 0.0001$, Kolmogorov-Smirnov with Sidak. D) Simplified schematic representation of the possible effects from (positive) noise correlations on the response separability of a theoretical population consisting of 2 units. E) Representative 2D linear discriminant projection of the simultaneously recorded response patterns of the 30 top ranked units from a mouse. F) 2D embedding of the 12D linear discriminant projection from the response patterns shown in (E), obtained using UMAP (*42*). G, H) Same as in F, but for modeled datasets minimizing noise correlations (decorrelated) or with scrambled responses, obtained by performing within-class randomization (G) and across class randomization (H) of the responses from the simultaneously recorded 30 top ranked units in the dataset shown in (F). I) Cumulative distribution plots of the absolute cross-validated single-trial prediction errors obtained using a Bayes classifier as a linear decoder (naive

approximation for computation efficiency) on the single-trial response patterns from the 7 top ranked units in the simultaneously acquired datasets across mice (cyan), modeled decorrelated datasets obtained by performing within-class randomization on the acquired data (orange) and the chance level distribution associated with our stimulation paradigm (gray).

Distribution of top ranked units across the imaged DCIC volume:

Previous studies mostly sampled and studied populations of azimuth sensitive units from the central nucleus region of the mammalian IC (CNIC) (*8*, *9*, *12*, *18*, *43*), leaving the behavior of populations at more dorsal IC subdivisions understudied. Our volumetric imaging approach allowed us to detect the presence of azimuth sensitive units (top ranked units) supporting a population code for sound location at the superficial 500 µm of the mouse DCIC (Fig. 1A). To further characterize this subpopulation of top ranked units, we studied how they are distributed across the imaged DCIC volume, which was positioned roughly at the center from the surface of the mouse dorsal IC (Fig. 1A, B). By comparing the positions of top ranked units to those of the complete samples of simultaneously imaged units across mice, we observed that the top ranked units (~32% from the complete DCIC populations imaged) are scattered across the imaged volumes following the same distributions across the anatomical axes of the complete imaged populations (Fig. 5). This observation suggests that the subpopulations of top ranked DCIC units associated with the population code of sound azimuth scatter across the DCIC without following a specific spatial pattern.

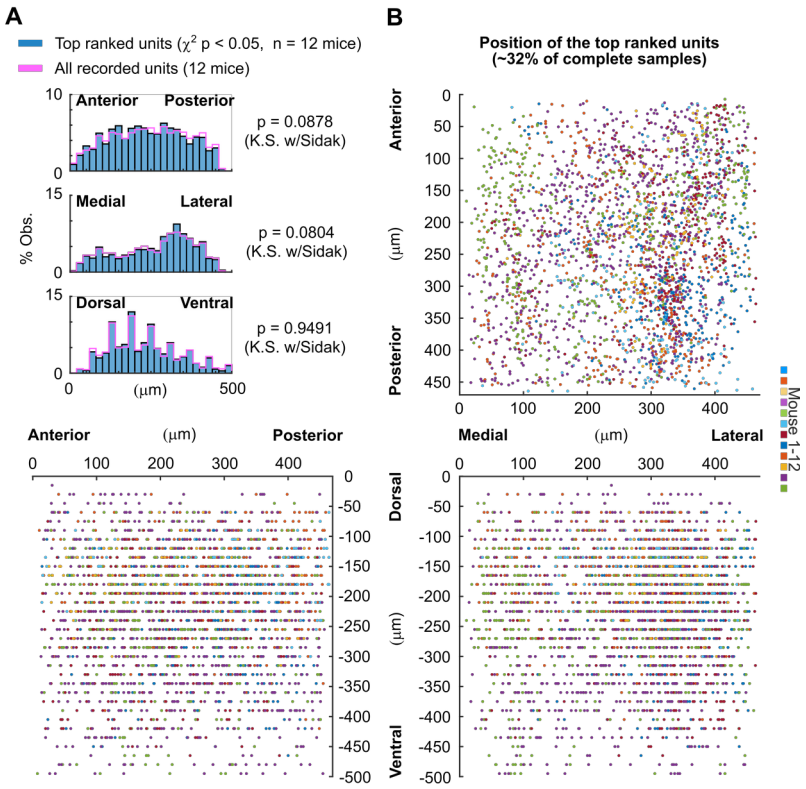

Figure 5: Top ranked units are scattered throughout the imaged DCIC volumes. A) Histogram plots of the distribution of top ranked unit position in the imaged volume across each anatomical axis (20 µm bins) obtained from all imaged mice, either for the complete sample of units (purple) or the subsample of top ranked units (~32% of all the units imaged per mice, blue). K.S.: Kolmogorov-Smirnov test. B) Scatter plots of the centroid position throughout the anatomical axes in the imaged volume from the detected top ranked units across mice.

Discussion

By performing fast volumetric Ca^{2+} imaging through sTeFo 2P microscopy (*21*), here we tackled the technical challenge to simultaneously record the activity of a large number of DCIC units in response to sound azimuth. We show that sTeFo 2P effectively achieved high throughput sampling across large imaging depths in a highly light-scattering tissue such as the mouse IC (Fig. 1), showcasing the capability of this method for interrogating neuronal population activity. Further improvements to this microscopy modality, including larger fields of view (*44–46*), multiplexing and 3P excitation (*47*), will open new horizons in the study of neuronal population function and systems neuroscience.

Despite the advantages of our imaging approach, our technique also has some limitations. In particular, large-scale volumetric imaging has a low temporal resolution, reaching sampling rates of 4 volumes per second, and requires the use of an indirect method of monitoring neuronal activity via Ca^{2+} sensors. The low temporal resolution effectively produces a low-pass filtering of neuronal activity, misrepresenting peak responses. Furthermore, indirectly inferring neuronal spiking responses from Ca^{2+} sensor signals can cause further information loss. Nevertheless, despite this information loss and misrepresentation of peak responses, the recorded population response patterns could be effectively classified with accuracies better than chance level and matching the behavioral discrimination ability of mice. This supports that our recordings still carried sufficient information about stimulus azimuth (Fig. 2, 3). Moreover, the information loss associated with our approach suggests that the actual achievable decoding errors are likely smaller than the ones observed in this study, potentially reaching levels that could be more precise than the behavioral performance, as reported in the visual system (*48*). Another aspect that could increase the prediction errors observed when decoding the recorded DCIC population responses is the presence of neurons with activities associated to non-auditory processes (*49*, *50*). Nevertheless, the detection and separation of these non-auditory responses are challenging due to the high trial-to-trial variability observed in our data, even for neurons with significant response dependency to stimulus azimuth. Another important limitation was that our custom microscope setup produced relatively high background SPL (79.5 dB SPL, see Methods), despite our efforts to isolate the head-fixed mouse under the objective in a sound attenuating chamber. Despite these limitations, this work showcases how volumetric Ca^{2+} imaging with 2-photon sTeFo microscopy can open new possibilities for future studies requiring high-throughput recordings of population activity to delimit and characterize specific subpopulations of units, especially considering the advantages brought by further technical improvements such as multiplexing or larger fields of view (*23*, *44–46*).

We targeted DCIC as this subdivision of IC is relatively understudied in the context of sound localization coding, partly because of technical difficulties to target the surface area of IC for electrophysiological recordings, and partly because there is no solid consensus on segmentation boundaries. Many discrepancies exist even between the most commonly used mouse brain reference atlases (*51*), like the Franklin-Paxinos atlas (*34*) and the Allen atlas (atlas.brain-map.org), which can lead to conflicting interpretations of experimental data (*52*). These differences could arise due to different criteria employed by

the neuroanatomists to segment anatomical subdivisions (histological stainings or magnetic resonance imaging), different tissue preparation methods (PFA fixed vs. fresh frozen) or intrinsic variability in the colonies of the animals employed (*51*). Here we adopted the IC segmentation boundaries and labels from the Franklin-Paxinos atlas, due to the extensive previous research employing it and the fact that we followed a compatible tissue preparation procedure for determining the anatomical location of our imaged volumes (PFA fixed tissue slices). Our large scale imaging potentially also reached the dorsal CNIC surface, in the deepest and central parts of the imaging volumes, and perhaps also ECIC in the more lateral and posterior side. Nevertheless, due to a lack of consensus segmentation boundaries, we did not attempt to exclude these areas from the analysis since most, if not all, of the imaged volumes were targeted to DCIC. Recent efforts implementing the widely used segmentation and labeling from the Franklin-Paxinos atlas into the Allen common coordinate framework represent a step forward to circumvent these issues (*51*).

The simultaneously imaged DCIC population responses from passively listening mice showed prominent trial-to-trial variation that rendered descriptive statistics such as response averages or medians and their tuning to stimulus azimuth little informative about what occurs on the single-trial basis (Fig 1, 3). Neurons with average response tuning to ILD have been detected at the mouse auditory cortex through *in vivo* 2P Ca^{2+} imaging (*10*), supporting that our observation is not due to a methodological caveat but is rather a property of DCIC populations. Nevertheless, we could still detect relevant subpopulations of DCIC units that showed significant dependency on stimulus azimuth (top ranked units), hence effectively encoding stimulus location in their single-trial response patterns with an accuracy that matches the discrimination ability of mice (*41*). Our findings suggest that sound azimuth information is redundantly distributed across the subpopulation of top ranked units, which points out that mechanisms beyond coding efficiency could be relevant for this population code. Our data show that the neuronal noise is often positively correlated across the simultaneous responses from pairs of top ranked units, and that these noise correlations can increase the separability between the single-trial subpopulation responses, contributing to the accuracy of the population code (Fig. 4). Thus, our data support the occurrence of a population code for sound azimuth at the mammalian IC as originally proposed by Day and Delgutte (2013), with data obtained with a different method (Ca^{2+} imaging instead of electrophysiology) and animal model (mice instead of rabbits) to study IC population responses simultaneously during single-trials (instead of approximating them through pooling non-simultaneous recordings), at a different anatomical IC subdivision (DCIC instead of CNIC).

At the CNIC of passively listening animals, it has been reported that sound azimuth is encoded by the response patterns of neuronal populations with average response tuning to azimuth (*12*, *18*, *43*). In our DCIC data, we detected subpopulations of units whose response patterns carried enough stimulus azimuth information to do so (top ranked units). These sound location sensitive DCIC units were detected based on response dependency to stimulus azimuth rather than average response tuning. This observation points out possible functional similarities and differences between DCIC and CNIC in terms of population coding and individual cell sensitivity to sound location. Moreover, this observation could have potentially exciting implications, as DCIC represents a higher order relay of the auditory pathway receiving more profuse descending corticofugal inputs involved in sound location information processing and learning (*27*–*31*).

Altogether, despite these differences, we show that sound location coding does indeed occur at DCIC, and that this follows a comparable mechanism to the characterized population code at CNIC (*18*).

The subpopulations of DCIC top ranked units that encode stimulus azimuth scattered across the imaged volume with no specificity in their location across the anatomical axes (Fig. 5). Interestingly, *in vivo* imaging studies report that the mouse dorsal IC processes sound frequency information topogaphically (tonotopy), showing a distinct tonotopic arrangement of neurons across the rostromedial-caudolateral and dorso-ventral axes (*49*, *53*). A hypothetical functional relationship between the distribution of sound location encoding DCIC neuronal subpopulations and these tonotopic gradients of sound frequency tuning could shed light into how the DCIC subpopulation code of sound azimuth relates to the duplex theory of sound location (*54*). Technical improvements realizing larger fields of view to interrogate the wide-stretching tonotopic DCIC map in simultaneous recordings would be key to fulfill this task (*44*, *45*).

It has been reported that the population responses of a single IC (unilateral recordings from CNIC) can produce a complete representation of sound location throughout the frontal hemifield (*12*, *18*). Our observations support this notion, showing that unilateral subpopulations of top ranked DCIC units carry enough information to generate a representation of the complete frontal hemifield that is accurate enough to match the discrimination ability of mice (*41*). Discrepancies with respect to unilateral lesion studies (*18*, *55*), suggesting that one IC would carry information about the contralateral hemifield only, could be explained by the loss of commissural interactions between both ICs that contribute to sound location processing (*56*). In this respect, we observed that the jRGECO1a-labeled neurons we imaged could project contralaterally (Fig. 1A, inset), suggesting that the imaged DCIC populations would be involved in commissural interactions. This is particularly interesting in the context of the opposing two channel model of sound location coding proposed for the mammalian auditory brainstem (*4*, *57*), which was ruled out for azimuth coding at CNIC (*18*), but could still be relevant for understanding DCIC population coding of sound location.

Noise correlations have been reported to occur at the mammalian CNIC and have a role in sound categorization (*17*), however their influence on the population code for sound location remained unexplored (*12*, *18*, *58*). We found that noise correlations are a relevant shaping force for the response patterns from DCIC subpopulations encoding sound location in passively listening mice (Fig. 4). These findings point out that response sensitivity to azimuth is not the main or only feature of IC neurons carrying information about stimulus azimuth, as considered in previous studies (*8*, *9*, *12*, *18*, *58*). This implication might extend to other brain regions relevant for sound location coding or different sensory modalities. More generally, the noise correlations observed across the imaged population responses highlight how these correlations can significantly influence population response separability and in consequence the encoding of sensory information, positioning their characterization across sensory modalities as a relevant step in the study of sensory information coding by neuronal populations (*15*).

In conclusion, our simultaneous recordings directly support that population response patterns at the mammalian IC encode sound location on the single-trial basis. Specifically, we report the presence of a

population code for sound azimuth at DCIC, in which azimuth information is redundantly distributed across a specific subset of azimuth sensitive units which scatter randomly across DCIC. Finally, this population code is robust against trial-to-trial variation with neuronal noise-correlations contributing to its accuracy.

Acknowledgements

We acknowledge Lina Streich and Ling Wang for their contribution to microscope assembly and setup, the mechanical and electronics workshops and the laboratory animal resource facility of EMBL Heidelberg for technical assistance. Evan Harrell for input on motorized speaker design and Jacques Bourg for input on IC cranial window surgeries. Peter Rupprecht and Alejandro Tlaie-Boria for helpful comments on the manuscript. JCB acknowledges supporting fellowships from the EMBL Interdisciplinary Postdoc (EIPOD) Programme under Marie Skłodowska Curie Cofund Actions MSCA-COFUND-FP (664726). This work was funded by the European Molecular Biology Laboratory (EMBL) and the Deutsche Forschungsgemeinschaft (DFG, German Research Foundation) – project 458898724 awarded to RP.

Competing interests

The authors declare no competing financial interests.

Materials & correspondence

Datasets and code are available upon reasonable request.

References

1. A. J. King, J. W. H. Schnupp, T. P. Doubell, The shape of ears to come: Dynamic coding of auditory space. *Trends Cogn. Sci.* **5**, 261–270 (2001).
2. E. I. Knudsen, M. Konishi, Mechanisms of sound localization in the barn owl (Tyto alba). *J. Comp. Physiol.* □ *A*. **133**, 13–21 (1979).
3. A. Kulkarni, H. S. Colburn, Role of spectral detail in sound-source localization. *Nature*. **396**, 747–749 (1998).
4. B. Grothe, M. Pecka, D. McAlpine, Mechanisms of Sound Localization in Mammals. *Physiol. Rev.* **90**, 983–1012 (2010).
5. R. A. Felix, B. Gourévitch, C. V. Portfors, Subcortical pathways: Towards a better understanding of auditory disorders. *Hear. Res.* **362**, 48–60 (2018).
6. J. K. Brunso-Bechtold, G. C. Thompson, R. B. Masterton, HRP study of the organization of auditory afferents ascending to central nucleus of inferior colliculus in cat. *J. Comp. Neurol.* **197**, 705–722 (1981).
7. J. C. Adams, Ascending projections to the inferior colliculus. *J. Comp. Neurol.* **183**, 519–538 (1979).
8. S. M. Chase, E. D. Young, Cues for sound localization are encoded in multiple aspects of spike trains in the inferior colliculus. *J. Neurophysiol.* **99**, 1672–1682 (2008).

9. S. M. Chase, E. D. Young, Limited segregation of different types of sound localization information among classes of units in the inferior colliculus. *J. Neurosci.* **25**, 7575–7585 (2005).

10. M. Panniello, A. J. King, J. C. Dahmen, K. M. M. Walker, Local and global spatial organization of interaural level difference and frequency preferences in auditory cortex. *Cereb. Cortex*. **28**, 350–369 (2018).

11. J. C. Clarey, P. Barone, W. A. Irons, F. K. Samson, T. J. Imig, Comparison of Noise and Tone Azimuth Tuning of Neurons in Cat Primary Auditory-Cortex and Medial Geniculate-Body. *J. Neurophysiol.* **74**, 961–980 (1995).

12. M. L. Day, B. Delgutte, Neural population encoding and decoding of sound source location across sound level in the rabbit inferior colliculus. *J. Neurophysiol.* **115**, 193–207 (2016).

13. A. P. Georgopoulos, A. B. Schwartz, R. E. Kettner, Neuronal Population Coding of Movement Direction. *Science (80-.).* **233**, 1416–1419 (1986).

14. A. P. Georgopoulos, J. F. Kalaska, R. Caminiti, J. T. Massey, ON THE RELATIONS BETWEEN THE DIRECTION TWO-DIMENSIONAL ARM MOVEMENTS AND CELL DISCHARGE PRIMATE MOTOR CORTEX1 IN. *J. Neurosci.* **2**, 1527–1537 (1982).

15. B. B. Averbeck, P. E. Latham, A. Pouget, Neural correlations, population coding and computation. *Nat. Rev. Neurosci.* **7**, 358–366 (2006).

16. A. Kohn, R. Coen-Cagli, I. Kanitscheider, A. Pouget, Correlations and Neuronal Population Information. *Annu. Rev. Neurosci.* **39**, 237–256 (2016).

17. M. Sadeghi, X. Zhai, I. H. Stevenson, M. A. Escabí, *A neural ensemble correlation code for sound category identification* (2019), vol. 17.

18. M. L. Day, B. Delgutte, Decoding Sound Source Location and Separation Using Neural Population Activity Patterns. *J. Neurosci.* **33**, 15837–15847 (2013).

19. J. W. Schnupp, a J. King, Coding for auditory space in the nucleus of the brachium of the inferior colliculus in the ferret. *J. Neurophysiol.* **78**, 2717–2731 (1997).

20. N. A. Lesica, A. Lingner, B. Grothe, Population coding of interaural time differences in gerbils and barn owls. *J. Neurosci.* **30**, 11696–11702 (2010).

21. R. Prevedel, A. J. Verhoef, A. J. Pernía-Andrade, S. Weisenburger, B. S. Huang, T. Nöbauer, A. Fernández, J. E. Delcour, P. Golshani, A. Baltuska, A. Vaziri, Fast volumetric calcium imaging across multiple cortical layers using sculpted light. *Nat. Methods*. **13**, 1021–1028 (2016).

22. J. J. Jun, N. A. Steinmetz, J. H. Siegle, D. J. Denman, M. Bauza, B. Barbarits, A. K. Lee, C. A. Anastassiou, A. Andrei, Ç. Aydin, M. Barbic, T. J. Blanche, V. Bonin, J. Couto, B. Dutta, S. L. Gratiy, D. A. Gutnisky, M. Häusser, B. Karsh, P. Ledochowitsch, C. M. Lopez, C. Mitelut, S. Musa, M. Okun, M. Pachitariu, J. Putzeys, P. D. Rich, C. Rossant, W. L. Sun, K. Svoboda, M. Carandini, K. D. Harris, C. Koch, J. O'Keefe, T. D. Harris, Fully integrated silicon probes for high-density recording of neural activity. *Nature*. **551**, 232–236 (2017).

23. S. Weisenburger, F. Tejera, J. Demas, B. Chen, J. Manley, F. T. Sparks, F. Martínez Traub, T. Daigle, H. Zeng, A. Losonczy, A. Vaziri, Volumetric Ca2+ Imaging in the Mouse Brain Using Hybrid Multiplexed Sculpted Light Microscopy. *Cell*. **177**, 1050-1066.e14 (2019).

24. C. Stringer, M. Pachitariu, N. Steinmetz, C. B. Reddy, M. Carandini, K. D. Harris, Spontaneous behaviors drive multidimensional, brainwide activity. *Science (80-.).* **364** (2019), doi:10.1126/science.aav7893.

25. J. Zhou, S. Shore, Convergence of spinal trigeminal and cochlear nucleus projections in the inferior colliculus of the guinea pig. *J. Comp. Neurol.* **495**, 100–112 (2006).

26. R. A. Felix, B. Gourévitch, C. V. Portfors, Subcortical pathways: Towards a better understanding of auditory disorders. *Hear. Res.* **362**, 48–60 (2018).

27. V. M. Bajo, A. J. King, Cortical modulation of auditory processing in the midbrain. *Front. Neural Circuits*. **6**, 1–12 (2012).

28. V. M. Bajo, F. R. Nodal, D. R. Moore, A. J. King, The descending corticocollicular pathway mediates learning-induced auditory plasticity. *Nat. Neurosci.* **13**, 253–260 (2010).

29. J. A. Winer, M. L. Chernock, D. T. Larue, S. W. Cheung, Descending projections to the inferior colliculus from the posterior thalamus and the auditory cortex in rat, cat, and monkey. *Hear. Res.* **168**, 181–195 (2002).

30. A. M. H. Lesicko, C. F. Angeloni, J. M. Blackwell, M. De Biasi, M. N. Geffen, Cortico-Fugal Regulation of Predictive Coding. *Elife*. **11**, 1–29 (2022).

31. V. M. Bajo, F. R. Nodal, C. Korn, A. O. Constantinescu, E. O. Mann, E. S. Boyden, A. J. King, Silencing cortical activity during sound-localization training impairs auditory perceptual learning. *Nat. Commun.* **10** (2019), doi:10.1038/s41467-019-10770-4.

32. H. Dana, S. Shoham, Numerical evaluation of temporal focusing characteristics in transparent and scattering media: erratum. *Opt. Express*. **20**, 28281 (2012).

33. B. R. Schofield, N. L. Beebe, Subtypes of GABAergic Cells in the Inferior Colliculus. *Hear. Res.* **376**, 1–10 (2019).

34. G. Paxinos, K. Franklin, *The Mouse brain in Stereotaxic Coordinates* (Academic Press, Second Edi., 2001).

35. T. Deneux, A. Kaszas, G. Szalay, G. Katona, T. Lakner, A. Grinvald, B. Rozsa, I. Vanzetta, Accurate spike estimation from noisy calcium signals for ultrafast three-dimensional imaging of large neuronal populations in vivo. *Nat. Commun.* **7** (2016), doi:10.1038/ncomms12190.

36. L. Huang, P. Ledochowitsch, U. Knoblich, J. Lecoq, G. J. Murphy, R. C. Reid, S. E. J. de Vries, C. Koch, H. Zeng, M. A. Buice, J. Waters, L. Li, Relationship between simultaneously recorded spiking activity and fluorescence signal in gcamp6 transgenic mice. *Elife*. **10**, 1–19 (2021).

37. P. Rupprecht, S. Carta, A. Hoffmann, M. Echizen, A. Blot, A. C. Kwan, Y. Dan, S. B. Hofer, K. Kitamura, F. Helmchen, R. W. Friedrich, A database and deep learning toolbox for noise-optimized, generalized spike inference from calcium imaging. *Nat. Neurosci.* **24**, 1324–1337 (2021).

38. G. Vanwalleghem, L. Constantin, E. K. Scott, Calcium Imaging and the Curse of Negativity. *Front. Neural Circuits*. **14**, 1–10 (2021).

39. M. Pachitariu, C. Stringer, K. D. Harris, Robustness of spike deconvolution for neuronal calcium imaging. *J. Neurosci.* **38**, 7976–7985 (2018).

40. M. Jazayeri, J. A. Movshon, Optimal representation of sensory information by neural populations. *Nat. Neurosci.* **9**, 690–696 (2006).

41. A. M. Lauer, S. J. Slee, B. J. May, Acoustic basis of directional acuity in laboratory mice. *JARO - J. Assoc. Res. Otolaryngol.* **12**, 633–645 (2011).

42. L. McInnes, J. Healy, J. Melville, UMAP: Uniform Manifold Approximation and Projection for Dimension Reduction. *arXiv*. **1802.03426** (2018) (available at http://arxiv.org/abs/1802.03426).

43. M. L. Day, K. Koka, B. Delgutte, Neural encoding of sound source location in the presence of a concurrent, spatially separated source. *J. Neurophysiol.* **108**, 2612–2628 (2012).

44. K. Ota, Y. Oisi, T. Suzuki, M. Ikeda, Y. Ito, T. Ito, H. Uwamori, K. Kobayashi, M. Kobayashi, M. Odagawa, C. Matsubara, Y. Kuroiwa, M. Horikoshi, J. Matsushita, H. Hioki, M. Ohkura, J. Nakai, M. Oizumi, A. Miyawaki, T. Aonishi, T. Ode, M. Murayama, Fast, cell-resolution, contiguous-wide two-photon imaging to reveal functional network architectures across multi-modal cortical areas. *Neuron*. **109**, 1810-1824.e9 (2021).

45. J. Demas, J. Manley, F. Tejera, K. Barber, H. Kim, F. M. Traub, B. Chen, A. Vaziri, *High-speed, cortex-wide volumetric recording of neuroactivity at cellular resolution using light beads microscopy* (2021), vol. 18.

46. M. Clough, I. A. Chen, S. W. Park, A. M. Ahrens, J. N. Stirman, S. L. Smith, J. L. Chen, Flexible simultaneous mesoscale two-photon imaging of neural activity at high speeds. *Nat. Commun.* **12**, 1–7 (2021).

47. S. Weisenburger, R. Prevedel, A. Vaziri, Quantitative evaluation of two-photon calcium imaging modalities for high-speed volumetric calcium imaging in scattering brain tissue. *bioRxivru*, 115659 (2017).

48. C. Stringer, M. Michaelos, D. Tsyboulski, S. E. Lindo, M. Pachitariu, High-precision coding in visual cortex. *Cell*. **184**, 2767-2778.e15 (2021).

49. A. B. Wong, J. G. G. Borst, Tonotopic and non-auditory organization of the mouse dorsal inferior colliculus revealed by two-photon imaging. *Elife*. **8**, 1–50 (2019).

50. K. G. Gruters, J. M. Groh, Sounds and beyond: Multisensory and other non-auditory signals in the inferior colliculus. *Front. Neural Circuits*. **6**, 1–39 (2012).

51. U. Chon, D. J. Vanselow, K. C. Cheng, Y. Kim, Enhanced and unified anatomical labeling for a common mouse brain atlas. *Nat. Commun.* **10** (2019), doi:10.1038/s41467-019-13057-w.

52. I. E. Bjerke, M. Øvsthus, K. A. Andersson, C. H. Blixhavn, H. Kleven, S. C. Yates, M. A. Puchades, J. G. Bjaalie, T. B. Leergaard, Navigating the murine brain: Toward best practices for determining and documenting neuroanatomical locations in experimental studies. *Front. Neuroanat.* **12**, 1–15 (2018).

53. O. Barnstedt, P. Keating, Y. Weissenberger, A. J. King, J. C. Dahmen, Functional Microarchitecture of the Mouse Dorsal Inferior Colliculus Revealed through In Vivo Two-Photon Calcium Imaging. *J. Neurosci.* **35**, 10927–10939 (2015).

54. L. Rayleigh, On our perception of sound direction. *Philos Mag*. **13**, 214–232 (1907).

55. W. M. Jenkins, B. Masterton, Sound Localization: Effects Of Unilateral Lesions in Central Auditory System. *J. Neurophysiol.* **47**, 978 (1982).

56. L. D. Orton, C. A. Papasavvas, A. Rees, Commissural Gain Control Enhances the Midbrain Representation of Sound Location. *J. Neurosci.* **36**, 4470–4481 (2016).

57. T. J. Park, A. Klug, M. Holinstat, B. Grothe, Interaural level difference processing in the lateral superior olive and the inferior colliculus. *J. Neurophysiol.* **92**, 289–301 (2004).

58. M. L. Day, K. Koka, B. Delgutte, Neural encoding of sound source location in the presence of a concurrent, spatially separated source. *J. Neurophysiol.* **108**, 2612–2628 (2012).

59. J. C. Boffi, J. Knabbe, M. Kaiser, T. Kuner, KCC2-dependent Steady-state Intracellular Chloride Concentration and pH in Cortical Layer 2/3 Neurons of Anesthetized and Awake Mice. *Front. Cell. Neurosci.* **12**, 1–14 (2018).

60. H. Dana, B. Mohar, Y. Sun, S. Narayan, A. Gordus, J. P. Hasseman, G. Tsegaye, G. T. Holt, A. Hu, D. Walpita, R. Patel, J. J. Macklin, C. I. Bargmann, M. B. Ahrens, E. R. Schreiter, V. Jayaraman, L. L. Looger, K. Svoboda, D. S. Kim, Sensitive red protein calcium indicators for imaging neural activity. *Elife*. **5**, 1–24 (2016).

61. A. Holtmaat, T. Bonhoeffer, D. K. Chow, J. Chuckowree, V. De Paola, S. B. Hofer, M. Hübener, T. Keck, G. Knott, W. C. A. Lee, R. Mostany, T. D. Mrsic-Flogel, E. Nedivi, C. Portera-Cailliau, K. Svoboda, J. T. Trachtenberg, L. Wilbrecht, Long-term, high-resolution imaging in the mouse neocortex through a chronic cranial window. *Nat. Protoc.* **4**, 1128–1144 (2009).

62. J. Schindelin, I. Arganda-Carreras, E. Frise, V. Kaynig, M. Longair, T. Pietzsch, S. Preibisch, C. Rueden, S. Saalfeld, B. Schmid, J. Y. Tinevez, D. J. White, V. Hartenstein, K. Eliceiri, P. Tomancak, A. Cardona, Fiji: An open-source platform for biological-image analysis. *Nat. Methods*. **9**, 676–682 (2012).

63. E. A. Pnevmatikakis, A. Giovannucci, NoRMCorre: An online algorithm for piecewise rigid motion correction of calcium imaging data. *J. Neurosci. Methods*. **291**, 83–94 (2017).

64. A. Giovannucci, J. Friedrich, P. Gunn, J. Kalfon, B. L. Brown, S. A. Koay, J. Taxidis, F. Najafi, J. L. Gauthier, P. Zhou, B. S. Khakh, D. W. Tank, D. B. Chklovskii, E. A. Pnevmatikakis, CaImAn an open source tool for scalable calcium imaging data analysis. *Elife*. **8**, 1–45 (2019).

Methods

- Animals and ethics statement:

This work was performed in compliance to the European Communities Council Directive (2010/63/EU) to minimize animal pain and discomfort. EMBL's committee for animal welfare and institutional animal care and use (IACUC) approved all experimental procedures under protocol number 2019-04-15RP. Experiments were performed on 7-16-week-old CBA/j mice obtained from Charles River Laboratories and housed in groups of 1-5 in makrolon type 2L cages on ventilated racks at room temperature and 50% humidity with a 12 hr light cycle. Food and water were available ad libitum.

- Surgical procedures:

Cranial window surgeries were performed on 7-8-week-old mice of either sex following procedures published elsewhere (*59*). Briefly, anesthesia consisted of a mixture of 40 µl fentanyl (0.1 mg/ml; Janssen), 160 µl midazolam (5 mg/ml; Hameln) and 60 µl medetomidin (1 mg/ml; Pfizer), dosed in 5 µl/g body weight and injected i.p.. Hair removal cream was used to remove the fur over the scalp of anesthetized mice and eye ointment was applied (Bepanthen, Bayer). 1% xylocain (AstraZeneca) was injected as preincisional anesthesia under the scalp. Prepared mice were then placed in a stereotaxic apparatus (David Kopf Instruments, model 963) with their bodies on a heating pad (37°C). The scalp was surgically removed to expose the dorsal cranium. The periosteum was removed with fine forceps and scissors to prepare the surface for cranial window implantation and stereotaxic delivery of viral vectors. Post-surgical pain relief was provided (Metacam, Boehringer Ingelheim) through s.c. injections (0.1 mg/ml, dosed 10µl/g body weight).

The Ca^{2+} indicator jRGECO1a (*60*) was expressed in IC neurons through induction with AAV vectors (Addgene #100854-AAV1), which were stereotaxically delivered as follows. A 4mm diameter circular craniectomy centered over IC (~1mm posterior to lambda (*34*)) was produced using a dental drill (Microtorque, Harvard Apparatus) with care to avoid bleeding and damage of the dura, which was not

removed and left intact. Stereotaxic injections were performed at the right IC (from bregma: -5.2 mm AP, 0.5 mm ML) with pulled glass pipettes lowered to depths of 300, 400 and 500 µm, at a rate of ~4ul/hr using a syringe. ~300nl were injected per site. After injection, the craniectomy was sealed with a round 4mm coverslip (~170µm thick, disinfected with 70% ethanol), with a drop of saline between the glass and the dura, and dental acrylic cement (Hager Werken Cyano Fast and Paladur acrylic powder). A head fixation bar was also cemented. The open skin wound was also closed with acrylic cement. At the end of the surgery anesthesia was antagonized with a subcutaneous injection of a mixture of 120 µl sterile saline, 800 µl flumazenil (0.1 mg/ml; Fresenius Kabi), and 60 µl atipamezole (5 mg/ml; Pfizer) dosed in 10 µl/g body weight. Mice were single housed after surgery and were allowed to recover for at least 4 weeks before imaging, providing time for Ca^{2+} indicator expression and for the inflammation associated with this surgery to resolve (*61*).

- sTeFo 2P microscopy:

We built a bespoke scanned temporal focusing (sTeFo) 2 photon microscope for fast volumetric in vivo Ca^{2+} imaging of large IC neuronal populations from awake mice. Technical details and detailed working principle are extensively described elsewhere (*21*). The main difference with respect to the microscope design published by Prevedel et al. (2016) was a higher repetition laser (10 MHz, FemtoTrain, Spectra Physics). Laser power while scanning was kept below 191 mW, measured after the objective, to avoid heating the brain tissue excessively (*21*). 470 μm^2 fields of view were imaged at 128 px^2 resolution and spaced in 15 µm z steps to cover 570 µm in depth (38 z steps) at a volume rate of 4.01 Hz. Artifacts produced by objective piezo z drive flyback were excluded from analysis.

In a typical imaging session, cranial window implanted mice were briefly (< 1 min) anesthetized with 5% isoflurane in O_2 for quick head fixation at a custom stage, slightly restraining their bodies inside a 5 cm diameter acrylic tube, and positioned under our custom 2P microscope. Mice fully recovered from the brief isoflurane anesthesia, showing a clear blinking reflex, whisking and sniffing behaviors and normal body posture and movements, immediately after head fixation. A pilot group of mice were habituated to the head fixed condition in daily 20 min sessions for 3 days, however we did not observe a marked contrast in the behavior of habituated versus unhabituated mice during our relatively short 25 min imaging sessions. In consequence imaging sessions never surpassed a maximum of 25 min, after which the mouse was returned to its home cage. Typically, mice were imaged a total of 2-11 times (sessions), one to three times a week.

- Sound Stimulation:

A custom sound-attenuating chamber was incorporated to the microscope setup, allowing only the objective to access the inside, to attenuate room and microscope scanner noise reaching the mouse. All possible sound reflecting surfaces were lined with 1 cm or 0.5 cm thick foam to preserve free-field conditions. SPL was measured using a free-field prepolarized measurement microphone (PCB Piezotronics, 378C01, with signal conditioner 482A21) placed on the setup stage in the position of the head of the mouse. Background R.M.S. SPL measurements during imaging without sound stimuli delivery were (in dB): 20-40 kHz: 79.5. For sound stimuli to be salient, their R.M.S. SPL was at least 10 dB above background R.M.S. SPL.

Sound stimuli consisted of 20-40 kHz broad-band white noise at 96.2 dB R.M.S. SPL, 500 ms in total duration including 10 ms up and down ramps. Sound stimuli were delivered through an electrostatic speaker (Tucker Davis Technologies, ES1 coupled to a ED1 speaker driver) mounted on an arm at an 8.5 cm distance away from the head of the mouse, which was mounted on a NEMA17 bipolar stepper motor (26 Ncm, 1.8 deg/step) placed under the head of the mouse to position the speaker around the frontal hemifield. The motor was controlled using an Arduino UNO microcontroller, running GRBL v0.9 (G-code interpreter, https://github.com/grbl/grbl) and coupled with the Arduino CNC Shield V3.10 (https://blog.protoneer.co.nz/arduino-cnc-controller/) running A4988 motor drivers. To control and program speaker positioning, we used the universal G-code sender (https://winder.github.io/ugs_website/). Synchronization of speaker positioning and sound stimulus delivery to data acquisition was done through a second Arduino UNO board receiving a scan start TTL from the microscope to trigger stimulation programs.

500 ms audio stimuli (including 10 ms up and down ramps) were synthesized using MATLAB (0.5 MHz sampling rate). Sound delivery was performed using a DAQ board (National Instruments, PXIe-6341) interfaced to MATLAB using the DAQmx wrapper from scanimage (https://vidriotechnologies.com/scanimage/).

A typical stimulation protocol consisted of a series of presentations of a sound stimulus in which azimuth angles varied randomly from 13 different frontal positions (frontal 180° split into 15° steps). Stimuli were presented every 5 seconds and each azimuth angle was presented on average 14 times per session. Minimum number of same-azimuth trials collected was 8.

- Ca^{2+}-imaging signal analysis:

Volumetric imaging data was visualized and rendered using FIJI (*62*). Motion correction was performed using NoRMCorre (*63*) on individual imaging planes from the volumetric datasets. jRGECO1a signal was extracted, denoised and neuropil corrected from each individual imaging plane using CaImAn (*64*). Spike probabilities were estimated using MLSpike (*35*).

- Histology:

At the end of the experiment mice were transcardially perfused with phosphate-buffered saline (PBS) followed by 4% paraformaldehyde at room temperature to fixate the brain. The perfused brain was dissected and post-fixed in 4% paraformaldehyde for 24 h at 4 °C. After post-fixation, brains were washed with PBS saline and stored at 4 °C. 100-µm-thick free-floating vibratome (Leica VT1200) coronal sections were cut at room temperature, mounted on slides using Vectashield with DAPI (H-1200-10, Vector Laboratories) and imaged in a NIKON Ti-E epifluorescence microscope equipped with a LUMENCOR SPECTRA X module for illumination, standard DAPI and mCherry filter cubes, and a pco.edge 4.2 CL sCMOS camera; using a CFI P-Apo 4x Lambda/ 0.20/ 20,00 objective.

- Statistical analyses:

Each mouse was considered a replicate. Datasets obtained in one imaging session from each mouse, consisting of ~200 azimuth trials were analyzed. We did not perform any form of data augmentation through resampling with restitution of the recorded responses to virtually increase the number of trials (*18*). Statistical

analyses were performed using MATLAB functions and custom scripts. For hypothesis testing, a p value < 0.05 was considered significant. Sidak's correction of p values was used for multiple comparisons. nS/N ratios were evaluated as the inverse of the coefficient of variation of the recorded responses of each cell across azimuth trials. Since many units failed to respond across many trials, we did not perform baseline spike probability subtraction as this frequently led to negative spike probabilities that were hard to interpret. One sided Kruskal-Wallis tests were performed to determine median response tuning to stimulus azimuth, with 12 degrees of freedom (13 tested azimuths). Two sample Kolmogorov-Smirnov and Wilcoxon rank sum tests were two sided. To find neurons with single-trial responses that were statistically dependent on stimulus azimuth (feature selection) we performed χ^2 independency tests using the function fscchi2 from the statistics and machine learning toolbox from MATLAB with default parameters, which binned the spike probability responses (continuous variable) into 10 bins. Cross validated sorting of noise correlation matrices was obtained by performing hierarchical clustering on half of the trials recorded based on pairwise neuronal noise correlations (using the Kendall tau as a non parametric correlation coefficient) as a distance metric, and plotting the pairwise correlation coefficient matrix registered for the other half of the trails, sorting the units based on the clustering. IC population response classification (decoding) was performed using the naive Bayes classifier algorithm implemented in MATLAB, using the fitcnb function from the statistics and machine learning toolbox. For the latter function, Bayesian hyperparameter optimization was employed to fit the models. For dimensionality reduction, feature selection and classification (decoding) a “leave one out” cross-validation strategy was implemented for the whole process, in which dimensionality reduction (PCA) or feature selection (top ranked cell selection, if applicable) was performed and then the models were fitted to the population responses collected in all trials except one (for each imaging session) and the one population response left out was decoded as is or using the selected features (best cells) or using the PCA loadings matrix to calculate PC scores, and fitted model. This procedure was iterated until all population responses collected were decoded (for each imaging session). The same cross-validation procedure was implemented for LDA (for data visualization, without the decoding step). For LDA, the MATLAB function fitcdiscr was used. Modeled datasets with decorrelated or scrambled responses were produced through within-class or across-class shuffling of the responses respectively. The decorrelated prediction error distribution was the cumulative outcome of 10 iterations of within-class shuffling of the responses from the datasets followed by decoding.